Article

Combined Reaction System for NH$_3$ Decomposition and CO$_2$ Methanation Using Hydrogen Permeable Membrane Reactor in 1D Model Analysis

Putri Permatasari [1], Haruka Goto [1], Manabu Miyamoto [2], Yasunori Oumi [2], Yogi Wibisono Budhi [3] and Shigeyuki Uemiya [2,*]

[1] Department of Material Science and Processing, Gifu University, Gifu 501-1113, Japan; putri.permatasari.s4@s.gifu-u.ac.jp (P.P.); harukagoto821@gmail.com (H.G.)
[2] Department of Chemistry and Biomolecular Science, Gifu University, Gifu 501-1113, Japan; miyamoto.manabu.v5@f.gifu-u.ac.jp (M.M.); oumi.yasunori.x2@f.gifu-u.ac.jp (Y.O.)
[3] Department of Chemical Engineering, Institut Teknologi Bandung, Bandung 40116, Indonesia; y.wibisono@itb.ac.id
[*] Correspondence: uemiya.shigeyuki.j8@f.gifu-u.ac.jp

Abstract: In a previous study, we developed an integrated reaction system combining NH$_3$ decomposition and CO$_2$ methanation within a membrane reactor, significantly enhancing reactor performance through efficient H$_2$ separation. Ru/Ba/γ-Al$_2$O$_3$ and Ru/ZrO$_2$ were employed as catalysts for each reaction. To ensure the accuracy and reliability of our results, they were validated through 1D models using FlexPDE Professional Version 7.21/W64 software. Key parameters such as reactor arrangement, catalyst bed positioning, overall heat transfer coefficient, rate constants, and H$_2$ permeance were investigated to optimize system efficiency. The study revealed that positioning the NH$_3$ decomposition on the shell side and CO$_2$ methanation on the tube side resulted in a better performance. Additionally, shifting the methanation catalyst bed downward by approximately one-eighth (10 mm from 80 mm) achieves the highest CO$_2$ conversion. A sensitivity analysis identified the rate constant of the NH$_3$ decomposition catalyst and the H$_2$ permeance of the membrane as the most influential factors in enhancing CO$_2$ conversion. This highlights the priority of improving membrane H$_2$ permeance and catalytic activity for NH$_3$ decomposition to maximize system efficiency.

Keywords: simulation; CO$_2$ methanation; NH$_3$ decomposition; Pd membrane reactor; combined reaction; reactor performance

1. Introduction

The reliance of humans on fossil fuels has driven rapid industrial growth since the 18th century, but at a high environmental cost [1,2]. Among the issues, global warming attributed to carbon dioxide (CO$_2$) constitutes 73.5% of the emissions and is the most critical, precipitating the alarming rise in temperatures and sea levels [3]. Corrective actions, such as altering land use, can reduce CO$_2$ emissions by 40–70 ppm (10–30% of emissions), and natural solutions like reforestation help, but are insufficient alone due to water and crop yield limitations [4–7]. Several global initiatives have been implemented, including the Kyoto Protocol and the Paris Agreement [6,8]. However, despite these initiatives, emissions remain beyond projected levels, highlighting the urgent need for effective emission reduction technology [6,9,10].

Carbon Capture, Utilization, and Storage (CCUS) is increasingly recognized as an effective way to reduce CO$_2$ emissions in various industries [9,11]. A notable advancement in this field is the methanation reaction, a procedure that employs CO$_2$ and hydrogen (H$_2$) to generate methane (CH$_4$)—a versatile substance widely employed in various applications [9,12,13]. Methane has significant potential as a clean energy source for the future, especially when produced as green methane using renewable energy rather than fossil

fuels [14–16]. The methanation process not only produces methane but also recycles CO_2, thereby reducing carbon emissions [14,17]. For this approach to remain sustainable, the hydrogen used should ideally be green hydrogen derived from renewable energy sources.

Chemical transformations reliant on H_2 face challenges due to costly H_2 storage and transportation [9,10,18]. Methods using liquid H_2, organic hydrides, and ammonia (NH_3) are being explored [9,10,19,20]. NH_3 stands out due to its H_2 density and LNG-like liquefaction compatibility, meaning that the strategy involves using renewable energy to generate hydrogen, converting it into NH_3 for storage and transport [9,21,22].

Hydrogen separation is essential to facilitate NH_3's role in hydrogen production [23]. Pd alloy-based inorganic membranes are highly efficient for hydrogen separation [24–26]. Electroless plating (ELP), the method used in this study, is the most common process, alongside chemical vapor deposition (CVD), physical vapor deposition (PVD), and electrodeposition (EPD) [27–33]. Membrane reactors play a crucial role in chemical process optimization by conducting reactions and separations simultaneously, improving both cost and energy efficiency [34,35]. The catalytic membrane method improves reaction selectivity and efficiency by manipulating thermodynamic equilibrium, isolating products, and enhancing purification and separation performance [35–38].

Significant progress has been made in NH_3 decomposition using membrane reactors, where hydrogen removal enhances conversion rates and reaction kinetics due to hydrogen permeation [39,40]. We have demonstrated a combined system of NH_3 decomposition and CO_2 methanation using a membrane reactor [41]. The hydrogen separation membrane enhances ammonia decomposition by removing H_2 from the system, and heat exchange between exothermic and endothermic reactions can save energy. Furthermore, using a membrane reactor to separate the two reactions increases the selectivity of the methanation reaction compared to mixing the two reactions in a single packed bed reactor, hence the use of a membrane reactor is favorable [41].

In system optimization, computational simulation is essential because it makes it possible to assess different operating conditions without the need for costly physical trials [42–47]. This covers sensitivity analyses and reaction kinetics computations. By combining catalyst and membrane data from previous research and employing computational methods to identify ideal settings, this work seeks to improve the combined system using a membrane reactor.

This research aims to address the urgent need to reduce greenhouse gas emissions and enhance hydrogen production efficiency. It concentrates on optimizing NH_3 decomposition and CO_2 methanation in a hydrogen-permeable membrane reactor. Efficiency is increased by the exothermic CO_2 methanation process, which supplies energy for the endothermic NH_3 decomposition. This study promotes scalable, affordable hydrogen production and aids in the fight against climate change by filling in gaps in the literature on catalyst performance, membrane separation, and heat transport and creating a simulation model to improve operations. This paper focuses on the computational analysis and simulation of a membrane reactor system for ammonia decomposition. Full experimental details regarding catalyst development, membrane fabrication, and system components can be found in our previous experimental study [41]. The current study builds on these experimental results to perform an in-depth computational analysis to optimize system performance and understand the reaction behavior.

2. Experimental Section

2.1. Determination of the Reaction Rate Formula

A $Ru/Ba/\gamma-Al_2O_3$ catalyst was used for the ammonia decomposition reaction. The exploration of NH_3 decomposition involved a systematic derivation of activation energy (E_A) and frequency factors (k_0). At the outset, the focus centered on selecting an appropriate model for this reaction. The Temkin–Phyzev model (Equation (1)) was deemed optimal, owing to its ability to provide a holistic overview of the reaction's trajectory. Drawing upon established reaction order values, where α is 1.410 and β is -1.176, a foundational basis

was established for the analysis [48–50]. For ammonia decomposition, a reverse reaction was not considered because the presence of a hydrogen-permeable membrane prevents a reverse reaction from occurring.

Moving forward, an understanding of the reaction rate equation for CO_2 methanation was also critical. For this reaction, a Ru/ZrO_2 catalyst and Lunde and Kester's model (Equation (2)) were used [51]. In this context, the consideration expanded to encompass the significance of the reverse reaction [52–57]. Reaction order values, where *n* is 0.85, were sourced from established studies [53]. Table 1 shows the experimental conditions used for determining the activation energy and frequency factor, as well as the experimental conditions used to determine the suitability of the reaction rate for the model. Figure 1 shows a schematic of the reaction equipment used in this system.

Table 1. Experimental conditions for determining reaction rate formula (in packed bed reactor).

|	Catalyst Performance			Model Suitability (W/F)					Model Suitability (Temp.)		
Catalyst weight (g)		0.5				2				0.5	
NH$_3$ flow rate (mL-stp/min)		40		145	67	30	23	16		40	
W/F (g.min/mol-$_{NH3}$)		280		308	668	1486	1945	2859		280	
Temperature (K)	623.15	673.15	723.15			623.15			623.15	673.15	723.15
Pressure (atm)		1				1				1	
Catalyst weight (g)		0.5				0.5				0.5	
CO$_2$/H$_2$ flow rate (mL-stp/min)		40/160		40/160	15/60	9/36	6/24	3/12		40/160	
W/F (g.min/mol-$_{CO2}$)		280		289	721	1186	1772	3475		280	
Temperature (K)	523.15	548.15	573.15			573.15			523.15 548.15	573.15 598.15	623.15 673.15
Pressure (atm)		1				1				1	
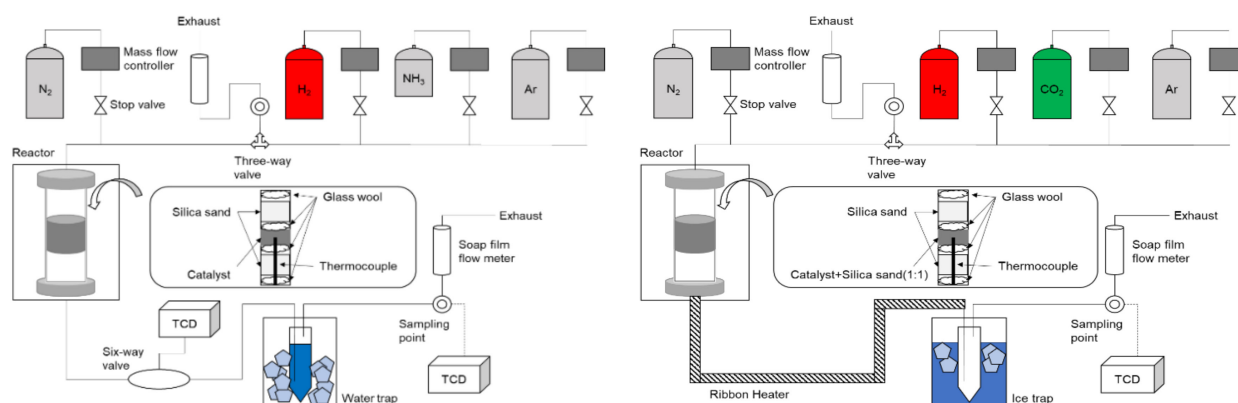
Figure 1. Schematic of reaction equipment used for NH_3 decomposition (**left**) and CO_2 methanation (**right**) reactor.

2.2. The Arrangement of the Reactors

A preliminary experimental study was conducted to establish a benchmark. The reaction conditions are shown in Table 2 and the dimensions of the system can be seen in Figure 2. The main equations used in this study are shown in Equations (1)–(12). Because we have two reactions in one system, there are two possible arrangements, as seen in Figure 1. Arrangement 1: CO_2 methanation in the tube, NH_3 decomposition in the shell. Arrangement 2: NH_3 decomposition in the tube, CO_2 methanation in the shell. These configurations significantly affect the heat transfer in the reactor, which crucial for the combined reaction system's efficiency. It is also important to note that the Pd layer is coated on the outer surface of the Al_2O_3 support. This point is crucial for determining the

membrane's area and the reactor's diameter measurements for each point. Following that, our membrane uses an asymmetric support with a small pore size on the outside and a large pore size on the inside. This has implications for the simulation's results. Assumptions included steady-state conditions, ideal gas behavior, and plug flow characteristics. The device's dimensions are shown in Figure 2, with membrane and catalyst layer lengths of 80 mm.

Table 2. Experimental conditions to determine the arrangement of the reactor.

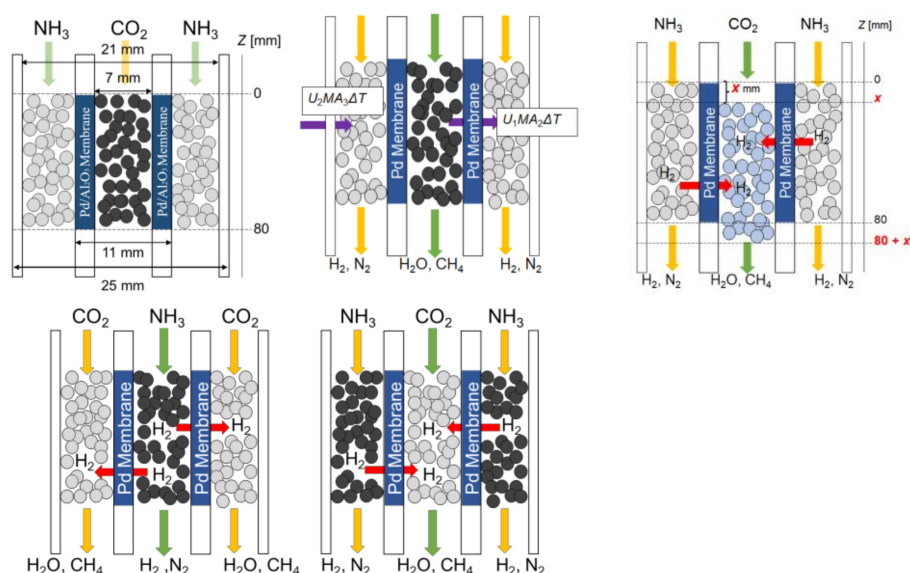| Inside catalyst weight (g)	1.5	**Arrangement 1**	
Outside catalyst weight (g)	10	heat transfer coefficients U_1 (W/m^2/K)	113.7
NH$_3$ flow rate (mL-stp/min)	40	heat transfer coefficients U_2 (W/m^2/K)	160.6
CO$_2$ flow rate (mL-stp/min)	15	**Arrangement 2**	
Reaction temperature (K)	623	heat transfer coefficients U_1 (W/m^2/K)	88.2
		heat transfer coefficients U_2 (W/m^2/K)	566.9

Figure 2. The device's dimensions (**upper left**), heat transfer in the system (**upper middle**), the position of the catalyst layer (**upper right**), and the arrangement of the reactors: arrangement 1 (**bottom left**) and arrangement 2 (**bottom right**).

FlexPDE Professional Version 7.21/W64 was used for calculations. A one-dimensional model was used, ignoring radial distribution and side reactions. Our results agree with Lundin et al.'s criteria for deciding whether to use 1D or 2D models in membrane reactors for hydrogen production [58]. They also assume the absence of axial and radial dispersion, which enhances the modeling technique for systems exhibiting such characteristics. The four key criteria considered are the Damköhler number (Da), Péclet number (Pe), transit parameter (θ), and equilibrium parameter (ε). In this study, the Péclet number (Pe) exceeds the critical Péclet number (Pe$_{crit}$), which confirms the validity of the 1D modeling approach. The model does not explicitly incorporate axial heat conduction, but it remains valid and provides valuable insights into the reactor system's behavior, as validated by experimental data. Physical property values used for simulation can be found in Table 3. The Table 4 presents the simulation conditions for the combined reaction within arrangements 1 and 2.

Table 3. Physical property values used for simulation.

d_1 [m]	7.00×10^{-3}		
d_2 [m]	1.10×10^{-2}		
d_3 [m]	2.10×10^{-2}		
d_4 [m]	2.50×10^{-2}		
d_p [m]	5.00×10^{-4}		
ε [-]	4.00×10^{-1}		
ε_w [-]	7.00×10^{-1}		
λ_al [W/m/K]	3.60×10^{1}		
λsus [W/m/K]	1.60×10^{1}		
λzr [W/m/K]	4.00×10^{0}		
Physical property value	**NH_3**	**N_2**	**H_2**
ai [J/mol/K]	2.79×10^{1}	3.12×10^{1}	2.71×10^{1}
bi [J/mol/K^2]	2.38×10^{-2}	-1.66×10^{1}	9.27×10^{-3}
ci [J/mol/K^3]	1.80×10^{-5}	2.68×10^{-5}	-1.88×10^{1}
di [J/mol/K^4]	-1.99×10^{1}	-1.97×10^{1}	7.65×10^{-9}
$\Delta H_{\mathrm{f},298K}$ [J/mol]	-4.71×10^{3}	0.00×10^{0}	0.00×10^{0}
M_w [g/mol]	1.70×10^{1}	2.80×10^{1}	2.02×10^{0}
K [Pas/K$^{0.5}$]	1.80×10^{-6}	1.38×10^{-6}	6.71×10^{-7}
C [K]	6.26×10^{2}	1.03×10^{2}	8.30×10^{1}
$\mu_{i,\,673\,K}$ [Pas]			
$\rho_0 i$ [kg/m^3]	7.71×10^{-1}	1.25×10^{0}	8.98×10^{-2}
Physical property value	**CO_2**	**CH_4**	**H_2O**
ai [J/mol/K]	1.98×10^{1}	1.93×10^{1}	3.22×10^{1}
bi [J/mol/K^2]	7.34×10^{-2}	5.21×10^{-2}	1.92×10^{-3}
ci [J/mol/K^3]	-6.10×10^{1}	1.20×10^{-5}	1.06×10^{-5}
di [J/mol/K^4]	1.72×10^{-8}	-1.93×10^{1}	3.60×10^{-9}
$\Delta H_{\mathrm{f},298K}$ [J/mol]	-4.06×10^{4}	-7.71×10^{3}	-2.49×10^{4}
M_w [g/mol]	4.40×10^{1}	1.60×10^{1}	1.80×10^{1}
K [Pas/K$^{0.5}$]	1.66×10^{-6}	1.08×10^{-6}	
C [K]	2.74×10^{2}	1.98×10^{2}	
$\mu_{i,\,673\,K}$ [Pas]			2.45×10^{-5}
ρ_0,i [kg/m^3]	1.98×10^{0}	7.17×10^{-1}	3.48×10^{-1}

Table 4. Simulation condition of combined reaction inside of arrangement 1 and 2.

SELECT		SELECT	
ngrid	1.00×10^{0}	ngrid	1.00×10^{0}
errlim	1.00×10^{-5}	errlim	1.00×10^{-5}
cell_limit	1.00×10^{2}	cell_limit	1.00×10^{2}

Table 4. *Cont.*

VARIABLES		VARIABLES	
F_{NH3}	1.00×10^{-9}	F_{NH3}	1.00×10^{-9}
$F_{H2(NH3)}$	1.00×10^{-9}	$F_{H2(NH3)}$	1.00×10^{-9}
F_{CO2}	1.00×10^{-9}	F_{CO2}	1.00×10^{-9}
$F_{H2(CO2)}$	1.00×10^{-9}	$F_{H2(CO2)}$	1.00×10^{-9}
T_{gc}	1.00×10^{-9}	T_{gc}	1.00×10^{-9}
T_{gn}	1.00×10^{-9}	T_{gn}	1.00×10^{-9}
DEFINITIONS		DEFINITIONS	
Z [m]	8.00×10^{-2}	Z [m]	8.00×10^{-2}
f_{NH3} [ml-stp/min]	4.00×10^{1}	f_{NH3} [ml-stp/min]	4.00×10^{1}
f_{CO2} [ml-stp/min]	1.50×10^{1}	f_{CO2} [ml-stp/min]	1.50×10^{1}
W_{in} [g]	1.50×10^{0}	W_{in} [g]	1.50×10^{0}
W_{out} [g]	1.00×10^{1}	W_{out} [g]	1.00×10^{1}
T_{g0} [K]	6.73×10^{2}	T_{g0} [K]	6.73×10^{2}
U_1 [W/m^2/K]	1.14×10^{2}	U_1 [W/m^2/K]	8.82×10^{1}
U_2 [W/m^2/K]	1.61×10^{2}	U_2 [W/m^2/K]	5.67×10^{2}
J [mol/m^2/s/Pa$^{0.5}$] [41]	1.71×10^{-4}	J [mol/m^2/s/Pa$^{0.5}$] [41]	1.71×10^{-4}
INITIAL VALUE		INITIAL VALUE	
F_{NH3}	$F_{NH3,0}$	F_{NH3}	$F_{NH3,0}$
$F_{H2(NH3)}$	$F_{H2(NH3),0}$	$F_{H2(NH3)}$	$F_{H2(NH3),0}$
F_{CO2}	$F_{CO2,0}$	F_{CO2}	$F_{CO2,0}$
$F_{H2(CO2)}$	$F_{H2(CO2),0}$	$F_{H2(CO2)}$	$F_{H2(CO2),0}$
T_{gc}	T_{g0}	T_{gc}	T_{g0}
T_{gn}	T_{g0}	T_{gn}	T_{g0}

Reaction rate

$$-r_{NH3} = k_{0,NH3}\, exp\left(\frac{-E_A}{RT}\right) \times P_{NH3}{}^{\alpha} P_{H2}{}^{\beta} \tag{1}$$

$$-r_{CO2} = k_{0,\,CO2}\, exp\left(\frac{-E_A}{RT}\right)\left\{ P_{CO2}{}^{n} P_{H2}{}^{4n} - \frac{P_{CH4}{}^{n} P_{H2O}{}^{2n}}{K_{eq}(T)^{n}} \right\} \tag{2}$$

Material Balance

$$\frac{dF_{NH3}}{dx} = A_{in}\rho_{cat}(-r_{NH3}) \tag{3}$$

$$\frac{dF_{H2(in)}}{dx} = 1.5 A_{in}\rho_{cat}(r_{NH3}) - Qi \tag{4}$$

$$\frac{dF_{CO2}}{dx} = A_{out}\rho_{cat}(-r_{CO2}) \tag{5}$$

$$\frac{dF_{H2(out)}}{dx} = 4 A_{out}\rho_{cat}(-r_{CO2}) + Qi \tag{6}$$

Heat Balance

- When ammonia decomposition is on the outside and carbon dioxide methanation is on the inside

$$\left(F_{NH3}C_{pm,NH3} + F_{H2}C_{pm,H2} + F_{N2}C_{pm,N2}\right)\frac{dT_{gn}}{dx} = A_{in}\rho_{cat}(-r_{NH3})(\Delta H_{R,T}) + U_1 M A_1\left(T_{gc} - T_{gn}\right) + U_2 M A_2\left(T_{g0} - T_{gn}\right) \tag{7}$$

$$\left(F_{CO2}C_{pm,CO2} + F_{H2}C_{pm,H2} + F_{CH4}C_{pm,CH4} + F_{H2O}C_{pm,H2O}\right)\frac{dT_{gc}}{dx} = A_{out}\rho_{cat}(-r_{CO2})(\Delta H_{R,T}) + U_1 M A_1\left(T_{gn} - T_{gc}\right) + C_{pm\,H2}Qi\left(T_{gn} - T_{gc}\right) \tag{8}$$

The overall heat transfer coefficient

$$\frac{h_w d_p}{\lambda_F} = \left(\frac{d_p}{d}\right)\left(\frac{\lambda_{er}}{\lambda_F}\right)\left\{a_1{}^2 + \frac{\Phi(b)}{\xi}\right\} \tag{9}$$

- The total heat transfer coefficient through the Pd membrane (U_1) [59] and the outer wall (U_2) [60]

$$\frac{1}{U_1 ZMA_1} = \frac{1}{h_{in} ZMA_1} + \frac{(d_2 - d_1)/2}{\lambda_{al} A_{m1}} + \frac{1}{h_{out} ZMA_2} \tag{10}$$

$$\frac{1}{U_2 ZMA_3} = \frac{1}{h_{out} ZMA_3} + \frac{(d_4 - d_3)/2}{\lambda_{sus} A_{m2}} \tag{11}$$

Hydrogen Permeation

$$Qi = J \times MA_1 \times \left(P_{H_2(in)}{}^{0.5} - P_{H_2(out)}{}^{0.5}\right) \tag{12}$$

2.3. Examination of Catalyst Layer Position

We aimed to optimize catalyst layer placement in the reactor by shifting the CO_2 methanation catalyst layer by x mm towards the gas outlet. The optimal arrangement is determined by comparing the total CO_2 conversion rates to maximize CO_2 utilization. Figure 1 (upper right) shows the settings used.

2.4. Parameter Change

We manipulated the reaction rate constant, hydrogen permeance, and total heat transfer coefficient to determine their impact on CO_2 conversion. These variables were chosen because of their critical roles in regulating reaction kinetics, material transport, and energy motion within the system. The initial variables were multiplied by a factor **a**, ranging from 0 to 25. The CO_2 conversion rate was used to assess the effects of these changes. Equations (1), (2) and (10)–(12) show the modified variables in red.

3. Results and Discussion

3.1. Determination of the Reaction Rate Formula

Figure 3 presents the determination of (E_A) and (k_0) for both reactions. For NH_3 decomposition, the Arrhenius plot analysis determined an E_A of 60.5 kJ/mol and a k_0 of 2.10×10^{-3} mol/g/s/$Pa^{\alpha+\beta}$. This value is in line with the literature which reports that the activation energy of the Ru/Al_2O_3 catalyst ranges from 60 to 90 kJ/mol, so even though it is lower, it is still considered valid for use in this study [59,61,62]. For CH_4 methanation, the analysis yielded an E_A of 100.4 kJ/mol and a k_0 if 1.35×10^{-16} mol/g/s/Pa^{5n}. Integrating these results into the established equations and comparing them with empirical data confirm that both formulas align with consistent trends, demonstrating their validity and applicability to the reaction kinetics.
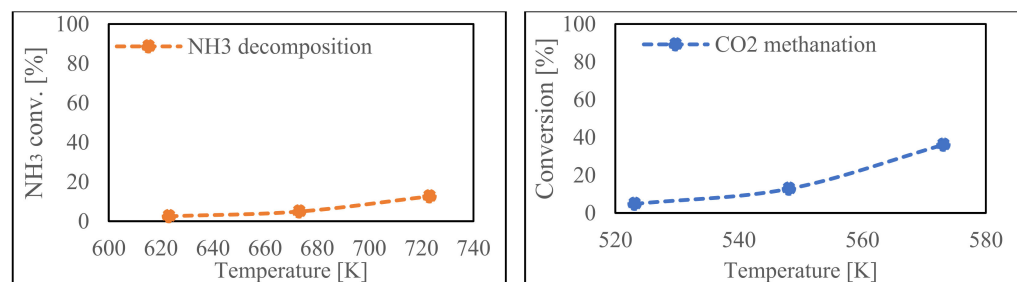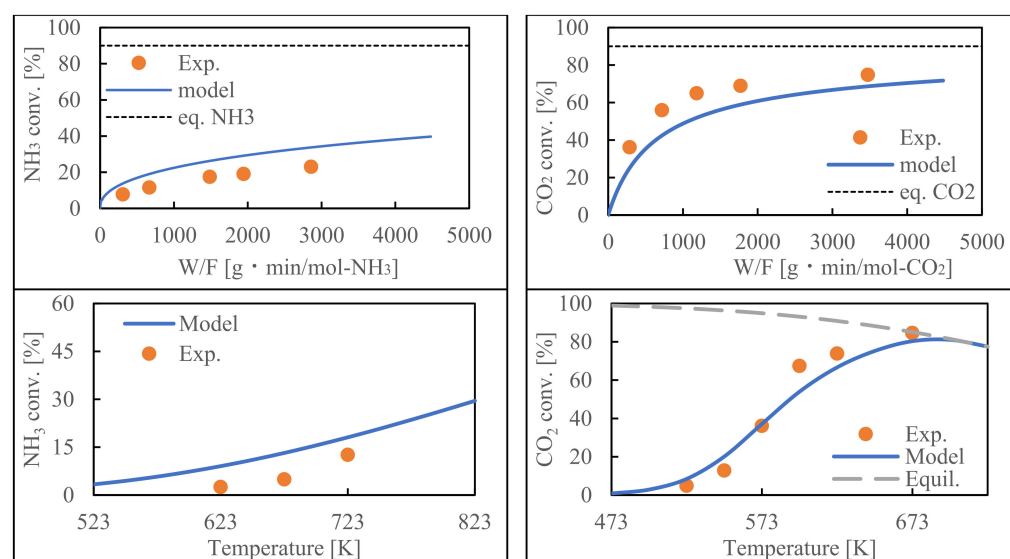

Figure 3. *Cont.*

Figure 3. Catalyst performance (**top**) and comparison of experimental and simulation results (**middle-bottom**) for ammonia decomposition reaction (**left**) and carbon dioxide methanation (**right**).

3.2. The Arrangement of the Reactors

Two options exist for the combined reaction setup: methanation on the shell side with decomposition on the tube side, or vice versa (Figure 2). The choice significantly impacts the system's behavior and outcomes, considering reaction kinetics, heat transfer, and efficiency. A preliminary experimental study was conducted to establish a basis for comparison and determine the practicality of the proposed configurations. The results revealed that arrangement 2 outperformed the other options (Figure 4(1)), supporting its potential for an improved performance. These findings add credibility to the subsequent simulation analyses and highlight the research's promising trajectory.

The model results aligned with experimental findings, showing arrangement 2 to be superior. Both reactions' conversion rates increased in this configuration (Figure 4(2)). This is due to NH_3 decomposition being the rate-determining step and placing it on the shell side allowed for a larger catalyst volume and increased hydrogen production, enhancing CO_2 methanation conversion. In addition, by placing the ammonia decomposition reaction, which is an endothermic reaction, closer to the heat source (in this case the reactor wall), the reaction will occur more easily so that the conversion in arrangement 2 is better than that in arrangement 1.

Based on the hydrogen pressure graph shown (Figure 4(3)), arrangement 2 shows a much higher hydrogen pressure on the NH_3 side reaching about 2.8 kPa, while arrangement 1 has a more balanced pressure distribution with a value of about 1.2–1.3 kPa on the NH_3 side and 0.5 kPa on the CO_2 side. Both arrangements show a significant increase in pressure at the beginning of the reactor (0–20 mm) before reaching a stable condition after 40 mm, but arrangement 2 produces a higher-pressure gradient between the two sides of the reactor which can increase the hydrogen transfer rate through the Pd membrane. This indicates that arrangement 2 is more effective for producing hydrogen from NH_3 decomposition, although the large pressure difference between the two sides can affect the efficiency of hydrogen transfer through the membrane, while arrangement 1 offers a more even pressure distribution which may be more beneficial for long-term operation stability.

The temperature profile graph in Figure 4(4) shows a clear difference between arrangement 1 and arrangement 2 during the combined reactions process. In arrangement 2, the temperature is higher, especially on the CO_2 side, reaching approximately 676 K. In contrast, arrangement 1 has a lower and more uniform temperature profile across both sides of the reactor. Both arrangements show a sudden drop and spike in temperature near the reactor's inlet (0–10 mm) before stabilizing. However, arrangement 2 creates a larger temperature difference between the NH_3 and CO_2 sides compared to arrangement 1.

This demonstrates that the arrangement of reactions significantly affects the temperature distribution in the reactor.
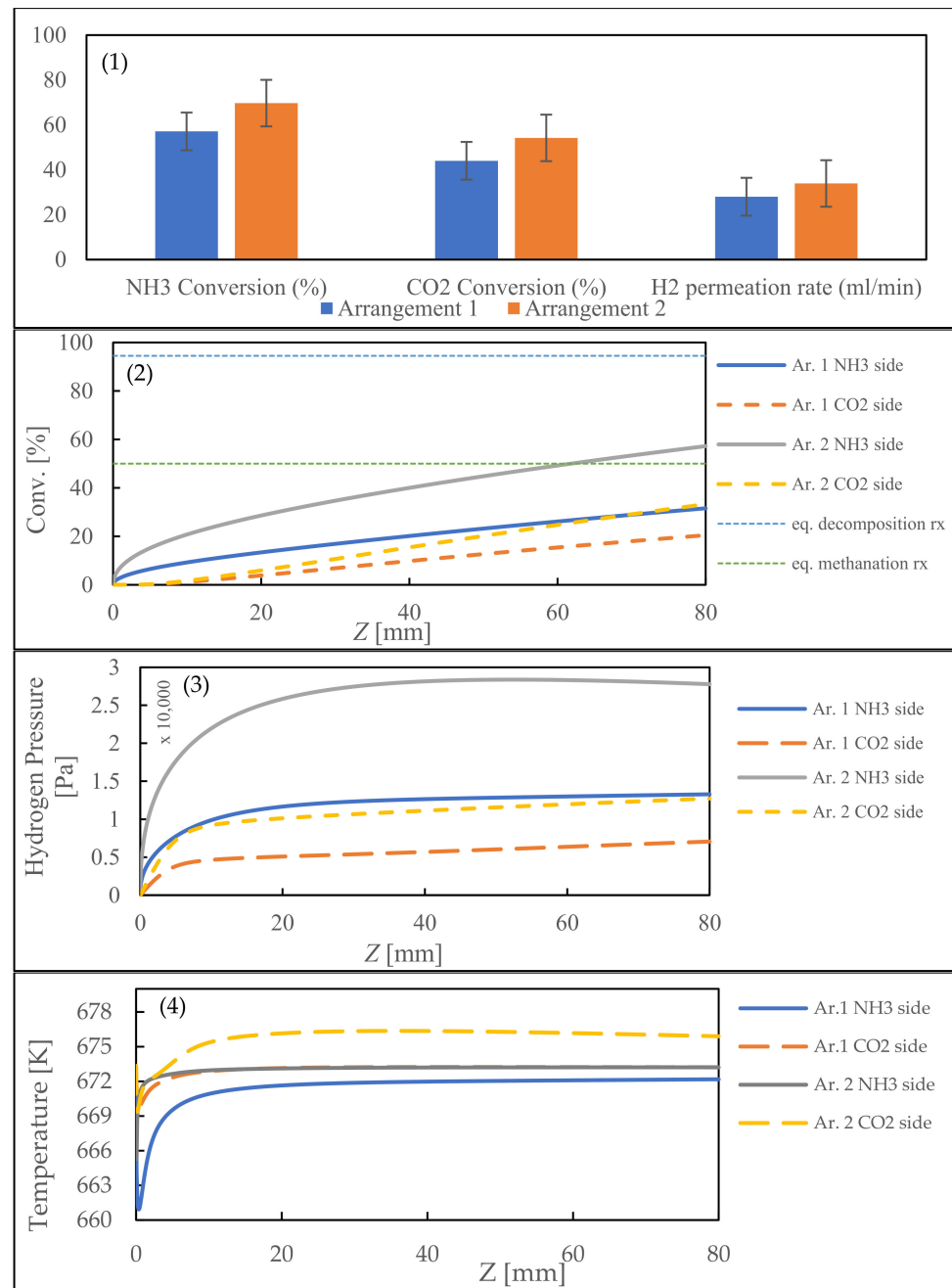

Figure 4. Experimental results (**1**) vs. simulated results for conversion rate (**2**), hydrogen pressure, (**3**) and temperature profile (**4**) obtained from arrangements 1 and 2.

Our analysis considers the heat transfer rate, temperature difference, thermal conductivity, and surface area. The heat transfer dynamics in arrangement 2 are shown in Figure 5. Negative values indicate heat release, while positive values indicate heat absorption. Upon closer examination, a notable trend occurs. Heat transfer through the outer reactor wall registers as being negative at approximately Z = 25 mm, indicating that heat is released from the shell side to the outer environment. This is intriguing considering that the decomposition reaction is endothermic which indicates that the methanation reaction on the tube side produces a significant amount of heat. This heat generation makes up for the heat absorbed by the decomposition reaction and produces extra amounts of heat that can

be discharged through the reactor wall. Near the reactor's entrance, a significant positive value emerges, possibly due to the initial interaction between NH_3 and the catalyst, causing a rapid start to the endothermic reaction. This region has a lower temperature than other sections. CO_2 methanation depends on H_2 being produced by the NH_3 decomposition. Even under outstanding conditions, compensating for the endothermic reaction's heat loss is not possible. Adopting this arrangement reduces heating costs, facilitates a more energy-efficient process, and makes it promising for long-term operations.
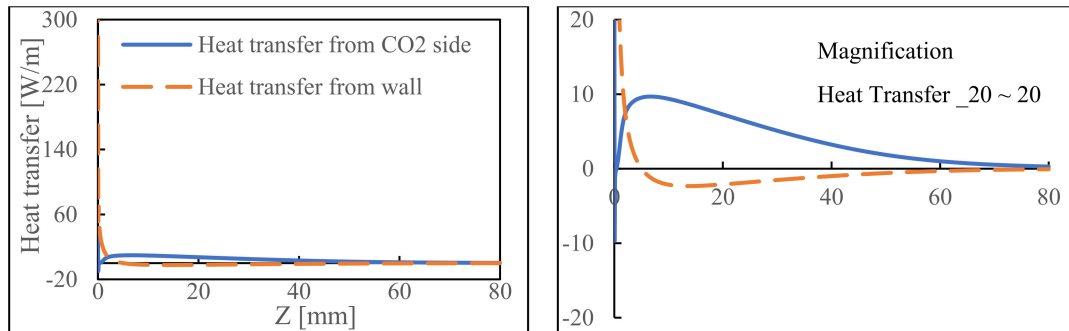
Figure 5. Heat transfer from arrangement 2 and its magnification.

3.3. Examination of Catalyst Layer Position

The conversion rate plot for the previous simulation (Figure 4(2)) shows lower CO_2 conversion rates near the entrance due to a limited hydrogen transmission from the NH_3 decomposition side. This suggests that the catalyst near the inlet was not optimally utilized, as reduced hydrogen availability limits its effectiveness. Proper catalyst utilization and hydrogen availability are crucial for reaction performance. Figure 6 shows the results after the catalyst layer has been displaced by x mm. The highest conversion rates are achieved when the CO_2 methanation catalyst is shifted between 9 and 13 mm. With an 80 mm catalyst bed height, the best positioning involves moving the CO_2 methanation catalyst downward by one-eighth of the total height, equivalent to a 10 mm displacement, producing optimal CO_2 conversion rates within the existing reactor configuration.
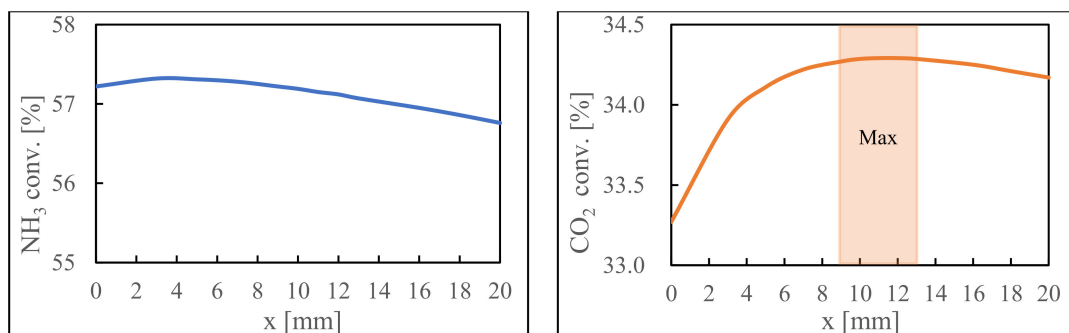

Figure 6. Conversion rates of both reactions when the CO_2 methanation catalyst is moved.

3.4. Parameter Change

An exploration of parameter variations was carried out to investigate the impact of several parameters on the system. This experiment looks at the effect of multiplying different variable values by a (0–25) on CO_2 conversion. The first stage of our investigation focused on the consequences of changes in the total heat transfer coefficient. In this regard, there are two separate heat transfer components: U_1, which represents heat transfer through the Pd film, and U_2, which represents heat transfer through the outer reactor wall. Figure 7 shows that neither form of heat transfer had a discernible impact on the CO_2 conversion rate. It was determined that, within the confines of the current reactor configuration, changes in heat transfer have no discernible effect on the overall CO_2 conversion rate. The

change in the heat transfer coefficient did not significantly affect CO_2 conversion, likely due to the predominance of other factors such as reaction kinetics and hydrogen permeation within the system. Additionally, the internal thermal balance between endothermic and exothermic reactions may contribute to the system's stability against variations in external heat transfer. These findings highlight the critical importance of optimizing catalysts and membranes, while still accounting for heat transfer considerations in the design of large-scale reactors.
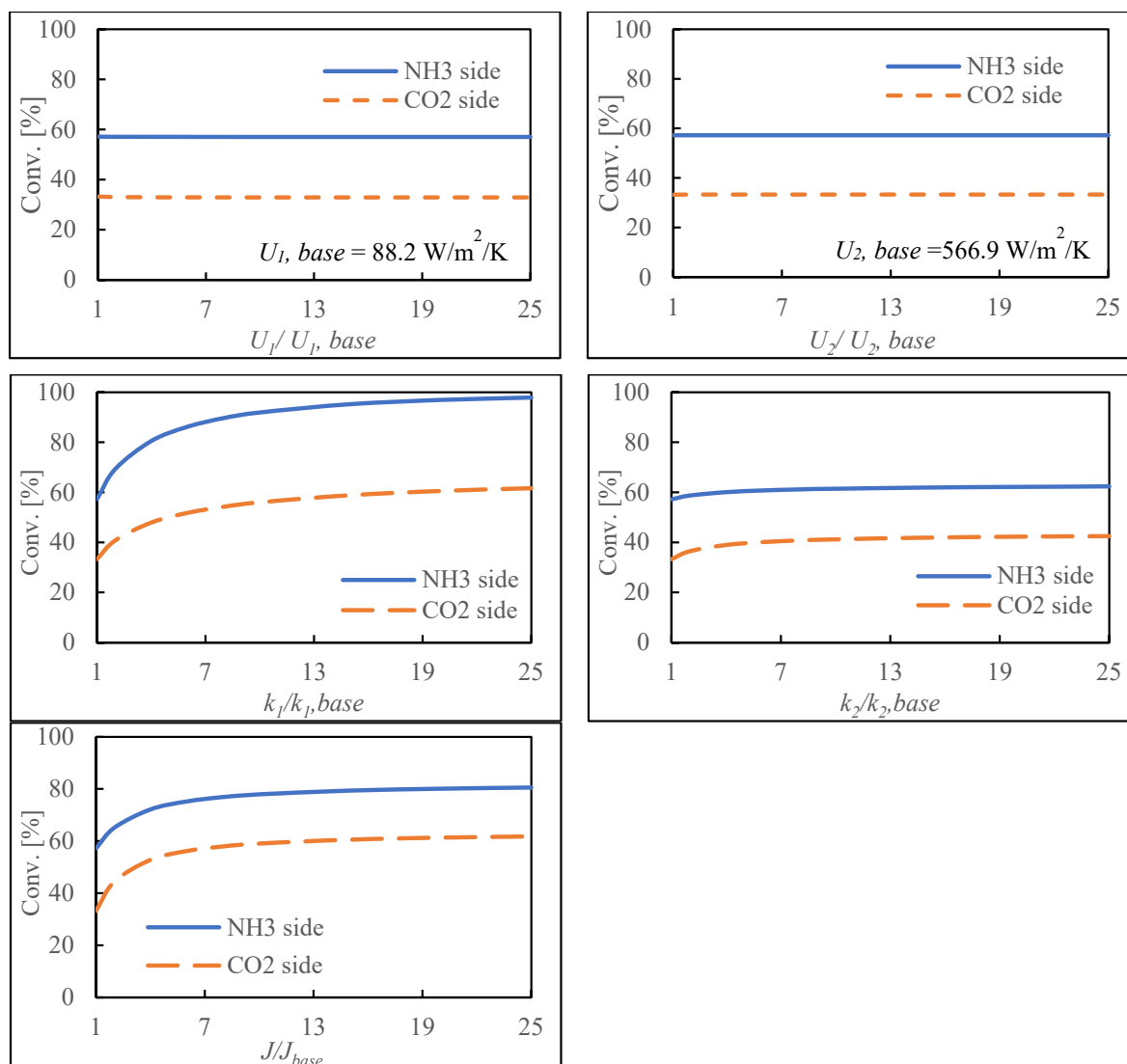
Figure 7. Effect of changes in heat transfer (**upper**), reaction rate constant (**middle**), and hydrogen permeance (**bottom**) on the system.

Figure 7 also shows the results for NH_3 and CO_2 conversion rates in response to variations in the reaction rate constant (*k*). An increase in the reaction rate constant has a clear consequence: increased conversion rates for both NH_3 decomposition (k_1) and CO_2 methanation reactions (k_2). It is important to remember that the decomposition reaction's reaction rate affects the system more. The efficiency of the methanation reaction is dependent on the quantity of hydrogen generated during NH_3 decomposition. Therefore, there is a bigger improvement in the conversion rate of the methanation reaction due to the rapid reaction rate in the decomposition phase greatly increasing the availability of hydrogen. This interaction highlights the complex relationship between reaction kinetics and reac-

tion interdependencies within the system, shedding light on strategic opportunities for improving system performance through the careful adjustment of reaction rate constants.

The results of varying hydrogen permeance (*J*) levels can also be seen. Notably, increasing the membrane's permeation capability accelerates the methanation reaction. This trend results from the direct relationship between membrane permeation and the kinetics of the H_2-CO_2 reaction. As membrane permeation increases, more hydrogen is available to interact with CO_2, increasing the overall conversion rate. This finding emphasizes the importance of hydrogen permeance in influencing the reaction dynamics within the system, as well as the potential for increasing the efficiency of the combined reaction process.

We also examined temperature variations for each sensitivity analysis parameter. However, these data were excluded because no significant temperature changes were seen. These findings imply that changing the examined parameters has little effect on the temperature profile in the reactor system.

The results as seen in Figure 8 support a key trend: changing the rate constant for NH_3 decomposition and increasing hydrogen permeance improves CO_2 conversion more than changing the rate constant for CO_2 methanation. This interesting observation shows that the CO_2 methanation catalyst's activity remains relatively high in its current configuration. The most important consideration is the critical roles of hydrogen production and permeance. Both factors emerge as significant determinants of the combined reaction system's efficiency. This emphasizes the importance of future endeavors, with a primary focus on developing better NH_3 decomposition catalysts and hydrogen permeation membranes. Increasing the efficiency of these critical components has the potential to significantly improve CO_2 conversion rates and overall reaction system performance, ushering in a new era of increased reaction kinetics and operational effectiveness.
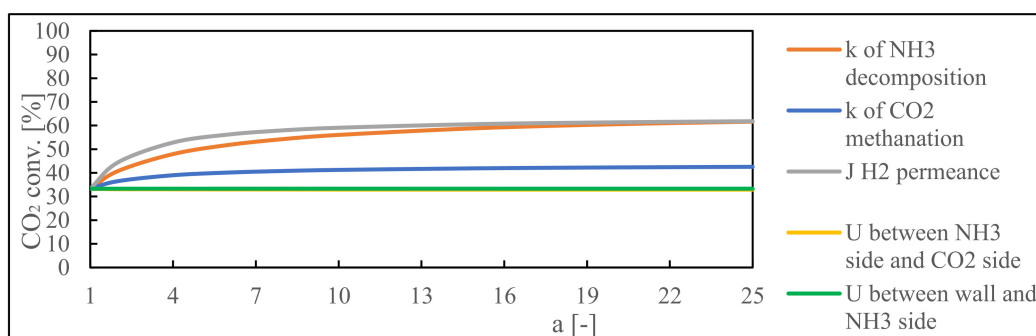

Figure 8. Sensitivity analysis of CO_2 conversion (combined) where a (0–25) is the sensitivity analysis variable.

4. Conclusions

This study offers important insights into the pathways for optimizing the reaction system, pinpointing catalyst placement and reactions as well as important elements that enhance overall operating efficiency. It was found that the carbon dioxide methanation on the tube side and the decomposition process on the shell side gave better results than the contrary. Strategically relocating the CO_2 methanation catalyst by about one-eighth of the catalyst layer's height resulted in a noticeable improvement in the system's efficiency. This result highlights how crucial catalyst positioning is to improve reaction kinetics. The greatest gains in efficiency were found when the rate constants for hydrogen permeance and NH_3 decomposition were increased. A hydrogen-permeable membrane and a more active NH_3 decomposition catalyst were shown to play crucial roles.

Author Contributions: Conceptualization, S.U. and M.M.; methodology, S.U., M.M., Y.W.B., H.G., P.P. and Y.O.; software, H.G. and Y.W.B.; validation, S.U. and M.M.; formal analysis, S.U., M.M., Y.W.B., Y.O., H.G. and P.P.; investigation, H.G.; resources, S.U. and M.M.; data curation, H.G.;

Nomenclature

Symbol	Description
$a, a_1{}^2, b, \xi, \Phi(b), \varphi$ [-]	Constant
A_n [m^2]	Cross-sectional area of n
A_{m1} [m^2]	Logarithmic mean area of membrane
A_{m2} [m^2]	Logarithmic mean area of reactor
α, β [-]	Reaction order of NH_3 decomposition
$C_{pm, i}$ [J/mol/K]	Molar heat capacity at constant pressure of component i
d, L [m]	Representative length
d_1 [m]	Inner diameter of membrane tube
d_2 [m]	Outer diameter of membrane tube
d_3 [m]	Inner diameter of reactor tube
d_4 [m]	Outer diameter of reactor tube
d_p [m]	Catalyst particle diameter
E_A [kJ/mol]	Activation energy
F_i [mol/s]	Molar flow rate of component i
h [W/m^2/K]	Heat transfer coefficient
h_w [W/m^2/K]	Heat transfer coefficient near the wall
J [mol/m^2/s/Pa$^{0.5}$]	H_2 permeance
K_{eq} [Pa^{-2}]	Equilibrium constant
k [mol/g/s/Pa$^\delta$]	Reaction rate constant
k_0 [mol/g/s/Pa$^\delta$]	Frequency factor
MA_2 [m]	Area outside the membrane per unit length of the reactor
MA_3 [m]	Area inside the reactor per unit length of the reactor
n [-]	Reaction order of CO_2 methanation
P_i [Pa]	Partial pressure of component i
Qi [mol/m/s]	H_2 flux per unit length of reactor
R [J/mol/K]	Gas constant $R = 8.314$
r_j [mol/g/s]	Reaction rate of reaction j
T [K]	Temperature
T_{g0} [K]	Reactor outer wall temperature
T_{gc} [K]	CO_2 side temperature
T_{gn} [K]	NH_3 side temperature
U [W/m^2/K]	Overall heat transfer coefficient
Z [m]	Length of height direction
$\Delta H_{R, T}$ [J/mol]	Enthalpy of reaction
λ_{al} [W/m/K]	Thermal conductivity of alumina
λ_{sus} [W/m/K]	Thermal conductivity of SUS tube
λ_{er} [W/m/K]	Effective thermal conductivity
ρ_{cat} [kg/m^3]	Density of catalyst bed

n = 1: inside the membrane, 2: outside the membrane, 3: inside the reactor, 4: outside the reactor
i = NH$_3$, CO$_2$, H$_2$, N$_2$, Ar, CH$_4$, H$_2$O
j = NH$_3$ decomposition, CO$_2$ methanation
δ = α + β (NH$_3$ decomposition), 5n (CO$_2$ methanation)

References

1. Hou, H.; Lu, W.; Liu, B.; Hassanein, Z.; Mahmood, H.; Khalid, S. Exploring the Role of Fossil Fuels and Renewable Energy in Determining Environmental Sustainability: Evidence from OECD Countries. *Sustainability* **2023**, *15*, 2048. [CrossRef]
2. Perera, F. Pollution from Fossil-Fuel Combustion is the Leading Environmental Threat to Global Pediatric Health and Equity: Solutions Exist. *Int. J. Environ. Res. Public Health* **2017**, *15*, 16. [CrossRef] [PubMed]
3. Perera, F.; Nadeau, K. Climate Change, Fossil-Fuel Pollution, and Children's Health. *N. Engl. J. Med.* **2022**, *386*, 2303–2314. [CrossRef] [PubMed]
4. Yin, C.; Pereira, P.; Zhao, W.; Barcelo, D. Natural climate solutions. The way forward. *Geogr. Sustain.* **2023**, *4*, 179–182. [CrossRef]
5. Friedlingstein, P.; Jones, M.W.; O'Sullivan, M.; Andrew, R.M.; Bakker, D.C.E.; Hauck, J.; Le Quéré, C.; Peters, G.P.; Peters, W.; Pongratz, J.; et al. Global Carbon Budget 2021. *Earth Syst. Sci. Data* **2021**, *13*, 655–679. [CrossRef]
6. Filonchyk, M.; Peterson, M.P.; Zhang, L.; Hurynovich, V.; He, Y. Greenhouse gases emissions and global climate change: Examining the influence of CO$_2$, CH$_4$, and N$_2$O. *Sci. Total Environ.* **2024**, *935*, 173359. [CrossRef]
7. Prentice, I.C.; Farquhar, G.D.; Fasham, M.J.R.; Goulden, M.L.; Heimann, M.; Jaramillo, V.J.; Kheshgi, H.S.; Le Quéré, C.; Scholes, R.J.; Wallace, D.W.; et al. The Carbon Cycle and Atmospheric Carbon Dioxide. In *Climate Change 2001: The Scientific Basis*; Cambridge University Press: Cambridge, UK, 2001; pp. 183–238.
8. Clémençon, R. The Two Sides of the Paris Climate Agreement: Dismal Failure or Historic Breakthrough? *J. Environ. Dev.* **2016**, *25*, 3–24. [CrossRef]
9. Nath, F.; Mahmood, M.N.; Yousuf, N. Recent advances in CCUS: A critical review on technologies, regulatory aspects and economics. *Geoenergy Sci. Eng.* **2024**, *238*, 212726. [CrossRef]
10. Jokar, S.M.; Farokhnia, A.; Tavakolian, M.; Pejman, M.; Parvasi, P.; Javanmardi, J.; Zare, F.; Gonçalves, M.C.; Basile, A. The recent areas of applicability of palladium based membrane technologies for hydrogen production from methane and natural gas: A review. *Int. J. Hydrogen Energy* **2023**, *48*, 6451–6476. [CrossRef]
11. Psarras, P.C.; Comello, S.; Bains, P.; Charoensawadpong, P.; Reichelstein, S.; Wilcox, J. Carbon Capture and Utilization in the Industrial Sector. *Environ. Sci. Technol.* **2017**, *51*, 11440–11449. [CrossRef]
12. Wang, W.; Zeng, C.; Tsubaki, N. Recent advancements and perspectives of the CO$_2$ hydrogenation reaction. *Green Carbon* **2023**, *1*, 133–145. [CrossRef]
13. Ridzuan, N.D.M.; Shaharun, M.S.; Anawar, M.A.; Ud-Din, I. Ni-Based Catalyst for Carbon Dioxide Methanation: A Review on Performance and Progress. *Catalysts* **2022**, *12*, 469. [CrossRef]
14. Biswas, S.; Kulkarni, A.P.; Giddey, S.; Bhattacharya, S. A Review on Synthesis of Methane as a Pathway for Renewable Energy Storage With a Focus on Solid Oxide Electrolytic Cell-Based Processes. *Front. Energy Res.* **2020**, *8*, 570112. [CrossRef]
15. Ingersoll, J.G. The Case of Renewable Methane by and with Green Hydrogen as the Storage and Transport Medium for Intermittent Wind and Solar PV Energy. *Hydrogen* **2024**, *5*, 209–229. [CrossRef]
16. Sun, T.; Shrestha, E.; Hamburg, S.P.; Kupers, R.; Ocko, I.B. Climate Impacts of Hydrogen and Methane Emissions Can Considerably Reduce the Climate Benefits across Key Hydrogen Use Cases and Time Scales. *Environ. Sci. Technol.* **2024**, *58*, 5299–5309. [CrossRef]
17. Tripodi, A.; Conte, F.; Rossetti, I. Carbon Dioxide Methanation: Design of a Fully Integrated Plant. *Energy Fuels* **2020**, *34*, 7242–7256. [CrossRef]
18. Allendorf, M.D.; Stavila, V.; Snider, J.L.; Witman, M.; Bowden, M.E.; Brooks, K.; Tran, B.L.; Autrey, T. Challenges to developing materials for the transport and storage of hydrogen. *Nat. Chem.* **2022**, *14*, 1214–1223. [CrossRef]
19. Zhang, T.; Uratani, J.; Huang, Y.; Xu, L.; Griffiths, S.; Ding, Y. Hydrogen liquefaction and storage: Recent progress and perspectives. *Renew. Sustain. Energy Rev.* **2023**, *176*, 113204. [CrossRef]
20. Makepeace, J.W.; He, T.; Weidenthaler, C.; Jensen, T.R.; Chang, F.; Vegge, T.; Ngene, P.; Kojima, Y.; de Jongh, P.E.; Chen, P.; et al. Reversible ammonia-based and liquid organic hydrogen carriers for high-density hydrogen storage: Recent progress. *Int. J. Hydrogen Energy* **2019**, *44*, 7746–7767. [CrossRef]
21. Kitano, M.; Inoue, Y.; Yamazaki, Y.; Hayashi, F.; Kanbara, S.; Matsuishi, S.; Yokoyama, T.; Kim, S.-W.; Hara, M.; Hosono, H. Ammonia synthesis using a stable electride as an electron donor and reversible hydrogen store. *Nat. Chem.* **2012**, *4*, 934–940. [CrossRef]
22. Ashida, Y.; Arashiba, K.; Nakajima, K.; Nishibayashi, Y. Molybdenum-catalysed ammonia production with samarium diiodide and alcohols or water. *Nature* **2019**, *568*, 536–540. [CrossRef] [PubMed]
23. Lider, A.; Kudiiarov, V.; Kurdyumov, N.; Lyu, J.; Koptsev, M.; Travitzky, N.; Hotza, D. Materials and techniques for hydrogen separation from methane-containing gas mixtures. *Int. J. Hydrogen Energy* **2023**, *48*, 28390–28411. [CrossRef]
24. Miller, J.B.; Morreale, B.D.; Smith, M.W. Pd-Alloy membranes for hydrogen separation. In *Reactor and Process Design in Sustainable Energy Technology*; Elsevier: Amsterdam, The Netherlands, 2014; pp. 135–161.
25. Cardoso, S.P.; Azenha, I.S.; Lin, Z.; Portugal, I.; Rodrigues, A.E.; Silva, C.M. Inorganic Membranes for Hydrogen Separation. *Sep. Purif. Rev.* **2018**, *47*, 229–266. [CrossRef]

26. Conde, J.J.; Maroño, M.; Sánchez-Hervás, J.M. Pd-Based Membranes for Hydrogen Separation: Review of Alloying Elements and Their Influence on Membrane Properties. *Sep. Purif. Rev.* **2017**, *46*, 152–177. [CrossRef]

27. Knapton, A.G. Palladium Alloys for Hydrogen Diffusion Membranes: A Review of High Permeability Materials. *Platin. Met. Rev.* **1977**, *21*, 44–50. [CrossRef]

28. Roa, F.; Block, M.J.; Douglas Way, J. The influence of alloy composition on the H_2 flux of composite Pd-Cu membranes. *Desalination* **2002**, *147*, 411–416. [CrossRef]

29. Li, A.; Liang, W.; Hughes, R. The effect of carbon monoxide and steam on the hydrogen permeability of a Pd/stainless steel membrane. *J. Membr. Sci.* **2000**, *165*, 135–141. [CrossRef]

30. Uemiya, S. Metal Membranes for Hydrogen Separation. *Membrane* **2005**, *30*, 13–19. [CrossRef]

31. Amandusson, H.; Ekedahl, L.G.; Dannetun, H. The effect of CO and O_2 on hydrogen permeation through a palladium membrane. *Appl. Surf. Sci.* **2000**, *153*, 259–267. [CrossRef]

32. Peters, T.; Caravella, A. Pd-based membranes: Overview and perspectives. *Membranes* **2019**, *9*, 25. [CrossRef]

33. Cerone, N.; Zito, G.D.; Florio, C.; Fabbiano, L.; Zimbardi, F. Recent Advancements in Pd-Based Membranes for Hydrogen Separation. *Energies* **2024**, *17*, 4095. [CrossRef]

34. Itoh, N. Membrane Reactors. *Membrane* **2006**, *31*, 14–15. [CrossRef]

35. Mamivand, S.; Binazadeh, M.; Sohrabi, R. Applicability of membrane reactor technology in industrial hydrogen producing reactions: Current effort and future directions. *J. Ind. Eng. Chem.* **2021**, *104*, 212–230. [CrossRef]

36. Wei, Y.; Liu, G.; Luo, J.; Li, L.; Xu, Z. Novel membrane separation technologies and membrane processes. *Front. Chem. Sci. Eng.* **2021**, *15*, 717–719. [CrossRef]

37. Westermann, T.; Melin, T. Flow-through catalytic membrane reactors-Principles and applications. *Chem. Eng. Process. Process Intensif.* **2009**, *48*, 17–28. [CrossRef]

38. Vankelecom, I.F.J. Polymeric membranes in catalytic reactors. *Chem. Rev.* **2002**, *102*, 3779–3810. [CrossRef]

39. Itoh, N.; Oshima, A.; Suga, E.; Sato, T. Kinetic enhancement of ammonia decomposition as a chemical hydrogen carrier in palladium membrane reactor. *Catal Today* **2014**, *236*, 70–76. [CrossRef]

40. Zhang, J.; Xu, H.; Li, W. High-purity COx-free H_2 generation from NH_3 via the ultra permeable and highly selective Pd membranes. *J. Membr. Sci.* **2006**, *277*, 85–93. [CrossRef]

41. Miyamoto, M.; Hayakawa, R.; Makino, Y.; Oumi, Y.; Uemiya, S.; Asanuma, M. CO_2 methanation combined with NH_3 decomposition by in situ H_2 separation using a Pd membrane reactor. *Int. J. Hydrogen Energy* **2014**, *39*, 10154–10160. [CrossRef]

42. Hafeez, S.; Al-Salem, S.M.; Constantinou, A. Membrane Reactors for Renewable Fuel Production and Their Environmental Benefits. In *Membranes for Environmental Applications*; Zhang, Z., Zhang, W., Lichtfouse, E., Eds.; Springer International Publishing: Cham, Switzerland, 2020; pp. 383–411. [CrossRef]

43. Wang, Y.; Shao, H.; Zhang, C.; Liu, F.; Zhao, J.; Zhu, S.; Leung, M.K.; Hu, J. Molecular dynamics for electrocatalysis: Mechanism explanation and performance prediction. *Energy Rev.* **2023**, *2*, 100028. [CrossRef]

44. Gallucci, F.; Fernandez, E.; Corengia, P.; van Sint Annaland, M. Recent advances on membranes and membrane reactors for hydrogen production. *Chem. Eng. Sci.* **2013**, *92*, 40–66. [CrossRef]

45. Simakov, D.S.A.; Sheintuch, M. Model-based optimization of hydrogen generation by methane steam reforming in autothermal packed-bed membrane reformer. *AIChE J.* **2011**, *57*, 525–541. [CrossRef]

46. Rahimpour, M.R.; Samimi, F.; Babapoor, A.; Tohidian, T.; Mohebi, S. Palladium membranes applications in reaction systems for hydrogen separation and purification: A review. *Chem. Eng. Process. Process Intensif.* **2017**, *121*, 24–49. [CrossRef]

47. Prašnikar, A.; Linec, M.; Jurković, D.L.; Bajec, D.; Sarić, M.; Likozar, B. Understanding membrane-intensified catalytic CO_2 reduction reactions to methanol by structure-based multisite micro-kinetic model. *J. Clean. Prod.* **2024**, *463*, 142480. [CrossRef]

48. Sayas, S.; Morlanés, N.; Katikaneni, S.P.; Harale, A.; Solami, B.; Gascon, J. High pressure ammonia decomposition on Ru-K/CaO catalysts. *Catal. Sci. Technol.* **2020**, *10*, 5027–5035. [CrossRef]

49. Chiuta, S.; Everson, R.C.; Neomagus, H.W.J.P.; Bessarabov, D.G. Hydrogen production from ammonia decomposition over a commercial Ru/Al_2O_3 catalyst in a microchannel reactor: Experimental validation and CFD simulation. *Int. J. Hydrogen Energy* **2016**, *41*, 3774–3785. [CrossRef]

50. Di Carlo, A.; Vecchione, L.; Del Prete, Z. Ammonia decomposition over commercial Ru/Al_2O_3 catalyst: An experimental evaluation at different operative pressures and temperatures. *Int. J. Hydrogen Energy* **2014**, *39*, 808–814. [CrossRef]

51. Lunde, P.J.; Kester, F.L. Rates of Methane Formation from Carbon Dioxide and Hydrogen Over a Ruthenium Catalyst. *J. Catal.* **1974**, *30*, 423–429. [CrossRef]

52. Falbo, L.; Martinelli, M.; Visconti, C.G.; Lietti, L.; Bassano, C.; Deiana, P. Kinetics of CO_2 methanation on a Ru-based catalyst at process conditions relevant for Power-to-Gas applications. *Appl. Catal. B* **2018**, *225*, 354–363. [CrossRef]

53. Ohya, H.; Fun, J.; Kawamura, H.; Itoh, K.; Ohashi, H.; Aihara, M.; Tanisho, S.; Negishi, Y. Methanation of carbon dioxide by using membrane reactor integrated with water vapor permselective membrane and its analysis. *J. Membr. Sci.* **1997**, *131*, 237–247. [CrossRef]

54. Wang, X.; Hong, Y.; Shi, H.; Szanyi, J. Kinetic modeling and transient DRIFTS–MS studies of CO_2 methanation over Ru/Al_2O_3 catalysts. *J. Catal.* **2016**, *343*, 185–195. [CrossRef]

55. Kiewidt, L.; Thöming, J. Predicting optimal temperature profiles in single-stage fixed-bed reactors for CO_2-methanation. *Chem. Eng. Sci.* **2015**, *132*, 59–71. [CrossRef]

56. Brooks, K.P.; Hu, J.; Zhu, H.; Kee, R.J. Methanation of carbon dioxide by hydrogen reduction using the Sabatier process in microchannel reactors. *Chem. Eng. Sci.* **2007**, *62*, 1161–1170. [CrossRef]

57. Solymosi, F.; Erdohelyi, A. Methanation of CO on Supported Rhodium Catalyst. *J. Catal.* **1980**, *68*, 371–382. [CrossRef]

58. Lundin, S.T.B.; Miklautz, M.; Ikeda, A.; Hasegawa, Y.; Ted Oyama, S. Criteria for the use of 1D and 2D models in catalytic membrane reactor modeling. *Chem. Eng. J.* **2023**, *477*, 147007. [CrossRef]

59. Yin, S.F.; Zhang, Q.H.; Xu, B.Q.; Zhu, W.X.; Ng, C.F.; Au, C.T. Investigation on the catalysis of COx-free hydrogen generation from ammonia. *J. Catal.* **2004**, *224*, 384–396. [CrossRef]

60. Bradford, M.C.J.; Fanning, P.E.; Vannice, M.A. Kinetics of NH_3 Decomposition over Well-Dispersed Ru. *J. Catal.* **1997**, *172*, 479–484. [CrossRef]

61. Armenise, S.; Cazaña, F.; Monzón, A.; García-Bordejé, E. In Situ generation of COx-free H_2 by catalytic ammonia decomposition over Ru-Al-monoliths. *Fuel* **2018**, *233*, 851–859. [CrossRef]

62. Lucentini, I.; Garcia, X.; Vendrell, X.; Llorca, J. Review of the Decomposition of Ammonia to Generate Hydrogen. *Ind. Eng. Chem. Res.* **2021**, *60*, 18560–18611. [CrossRef]